Flux-balanced Two-Field Plasma Edge Turbulence in a Channel Geometry

Di Qi[1, a)] and Andrew J. Majda[1, b)]

Department of Mathematics and Center for Atmosphere and Ocean Science, Courant Institute of Mathematical Sciences, New York University, New York, NY 10012

(Dated: 11 November 2019)

We investigate the drift wave – zonal flow interaction formulated on a more realistic channel domain geometry approximating the plasma turbulence near the tokamak edge regime. The recent two-field flux-balanced Hasegawa-Wakatani (BHW) model with improved treatment for parallel electron responses is adapted to the channel geometry with generalized zonal state structures. New conserved quantities are constructed based on the channel geometry to help the analysis for the competition between zonal states and non-zonal fluctuations. Effective bounds can be found constraining the maximum growth of total fluctuations and the amplitude of the dominant zonal state based on the conserved quantities. Total statistical variance among all the modes can be also estimated depending on the zonal state strength. The theoretical discoveries are confirmed by detailed numerical experiments from simulations in the channel domain. In addition, the channel geometry provides further support for the important advantage of adopting the balanced flux correction in the BHW model by showing a physically consistent growth rate from a stability analysis for the small-amplitude fluctuation interaction with a zonal mean state, in comparison with the modified Hasegawa-Wakatani model. This is again verified by direct numerical simulation results of the two models. The channel domain BHW model framework with the attractive features implies many potential applications in the study of the complex phenomena in plasma edge turbulence.

[a)]qidi@cims.nyu.edu

[b)]jonjon@cims.nyu.edu

I. INTRODUCTION

Near the edge regime of tokamak-type plasmas, the magnetic field exhibits a large level of variability in the zonal flows as well as ion density fluctuations from a number of experiments and simulations[1–5]. Understanding the formation of the zonal flow and its interaction with the non-zonal fluctuations from unstable drift waves is an active topic for the study of magnetically confined plasmas in tokamak edge regime[3,6–8]. The zonal flow – drift wave interaction is known to have strong effect in the heat and particle transport perpendicular to the magnetic surfaces and thus is crucial for the design of more reliable fusions devices. The adoption of simplified reduced fluid models enjoys the advantage in improving our understanding of the key interacting dynamics where the most relevant physical mechanism is identified.

One useful simplified formulation for the complex toroidal plasmas in the edge regime is provided by the Hasegawa-Wakatani (HW) models[9,10] by describing resistive drift waves in an intermediate regime between adiabatic and hydrodynamic electrons. The drift wave – zonal flow coupling is described by an interacting two-field evolution with self-induced drift instability on an embedded two-dimensional slab geometry[11–13]. In the models, the original toroidal magnetic geometry is flattened on a Cartesian coordinate x-y plane with x representing the radial direction and y as the poloidal direction. A *flux-balanced Hasegawa-Wakatani* (BHW) model is proposed in Refs. 14 and 15. This model guarantees a balanced treatment for the electron responses parallel to the magnetic field lines that provides many striking new features such as enhanced persistent zonal jets and stronger variability in fluctuations among a variety of dynamical regimes in the plasma field[14–17]. In comparison, the *modified Hasegawa-Wakatani* (MHW) model proposed in Ref. 18 lacks such skills in maintaining the strong zonal structures and shows transition to fully homogeneous drift turbulence. However, all the models are always defined on a doubly periodic domain for both the radial and poloidal directions only for the sake of computational convenience.

In this paper, we investigate the zonal flow – drift wave interaction in plasma edge turbulence using the BHW model on a new channel domain geometry. Periodic boundary is assumed only along the poloidal y direction in agreement with the circular symmetry, while a solid wall boundary is applied along the radial x direction representing the boundary walls in the tokamak edge regime. The channel geometry is obviously more realistic and provides a more physically feasible treatment for the computational geometry in the plasma edge regime of interest. Adopting the channel domain geometry also provides us the convenience to introduce large-scale zonal mean profiles in the density field Nx and the flow velocity Vx on top of the disturbance fields of particle density and electrostatic potential. These linear profiles are consistent with the observed structures

from direction channel domain simulation solutions. The imposed large-scale zonal states enable us to carry out a more detailed analysis for induced growth in flow interactions with the non-zonal fluctuations.

More importantly, new conserved quantities emphasizing the zonal mean state are discovered based on the channel domain geometry. Dynamical equations for the impulse functions as the first moments of the zonal states are derived depending on the zero particle transport across the radial boundaries. This new set of equations offers a direct link to the total particle flux appearing in both the total enstrophy and energy dynamics. With a proper combination of the dynamical equations, useful new conserved quantities can be constructed for the analysis of typical flow properties in zonal and fluctuation states. Especially, effective bounds can be found to give an accurate quantification of the saturated growth in the total fluctuations excited by drift instability from small initial states, as well as the amplitude in dominant zonal states generated by secondary transfer of energy from the excited fluctuation modes[16]. Statistical estimations in the total variance of flow ensemble solutions are also developed from the combination of the statistical impulse and enstrophy/energy equations. This balance between mean zonal states and total variance in fluctuations provides one potential way to interpret the role of zonal flows in quenching the impulsive particle transport, such as in the Dimits shift[19,20]. Detailed numerical simulations using the channel geometry are carried out to provide a direct confirmation of the theoretical estimations derived from the new conserved quantities. Efficient pseudo-spectral scheme developed for the doubly periodic domain[15] can be adapted for simulations in the channel domain case. Interesting new features are displayed in comparison with the original doubly periodic results. The numerical results confirm the accurate prediction of the growth trend from the theoretical formulas especially in the turbulent regime. The channel flow solutions with different aspect ratios for longer channel lengths are also compared, showing more regularized zonal jets with weaker time variability also consistent with the previous theoretical implications.

In addition, the channel geometry also provides better characterization for the improved treatment of electron response dynamics in the BHW model, compared with the limitations in the MHW model. The important advantage in the BHW model formulation in contrast to the MHW model without the balanced flux on the magnetic surfaces becomes more obvious in the channel flows. First, the non-trivial impulse relations are difficult to recover from the MHW model framework, so that the effective results for characterizing zonal state and fluctuation bounds discussed in the BHW model case are no longer valid. Second and more importantly, instability analysis for the zonal density state gives distinct results from the BHW and MHW models. Direct numerical simulations reveal a linear zonal profile in the density field. The BHW model leads to physically reasonable performance with strong instability in decaying density structure towards the boundary and stability for increasing density structure to withhold further radial transport. In contrast, the MHW model keeps

generating strong instability to increase the zonal particle transport no matter increasing or decreasing zonal density profiles. The crucial difference from instability analysis based on small-amplitude perturbations is further confirmed by direct numerical results of the BHW and MHW models.

In the structure of this paper, the generalized formulation of the BHW model on the channel domain is first described in Section II. The equations for the enstrophy and energy as well as the zonal mean dynamics are rederived based on the new channel geometry. New conserved quantities based on the impulse functions are introduced in Section III followed by the useful saturations bounds for zonal states and fluctuations as well as the statistics in equilibrium. The channel flow structures are illustrated by direct numerical simulations next in Section IV. The crucial difference in the BHW and MHW models in the channel domain with a background zonal profile is discussed in Section V. We summarize our results in Section VI and suggest directions for future work.

II. FORMULATION OF THE GENERALIZED HASEGAWA-WAKATANI MODEL IN A CHANNEL DOMAIN

Here, we provide a generalized formulation for the HW models based on the set of equations for the full field variables of the normalized potential vorticity q and particle density field n

$$\begin{aligned} \frac{\partial q}{\partial t} + \mathbf{v}_E \cdot \nabla q &= \mu \Delta q, \\ \frac{\partial \rho}{\partial t} + \mathbf{v}_E \cdot \nabla \rho &= \alpha \left(\tilde{\phi} - \tilde{\rho} \right) + \mu \Delta \rho. \end{aligned} \tag{1}$$

In the above model formulation, we define the total electrostatic potential function ϕ and the total particle density ρ for the full fields composed of a large-scale base state (V,N) and a disturbance component (φ,n) such that

$$\begin{aligned} \phi &= Vx + \varphi, \\ \rho &= Nx + n. \end{aligned} \tag{2}$$

N is the additional zonal density gradient characterizing the base zonal profile in density field. The full $\mathbf{E} \times \mathbf{B}$ velocity field $\mathbf{v}_E$ is defined by the potential function with a background zonal flow V along the poloidal direction and fluctuation component (u,v) on the two-dimensional domain

$$\mathbf{v}_E = \nabla^{\perp} \phi = (u, V + v),$$

where $\nabla^{\perp} = (-\partial_y, \partial_x)$ denotes the orthogonal gradient operator. For the other model parameters, κ determines the scale length of the background density gradient in an unchanging exponential profile; the adiabaticity

parameter α is proportional to the inverse of parallel resistivity describing the parallel current that destabilizes the system; and μ acts on the vorticity and density equations with a Laplace operator to approximate collisional ion viscosity perpendicular to the magnetic field[10,11]. The resistivity term on the right hand side of (1) acts on the fluctuation component $\tilde{f}$ by removing the zonally-averaged mean $\overline{f}$ from the original state variable denoted by f

$$\overline{f}(x) = \frac{1}{L_y}\int f(x,y)\,dy, \quad \tilde{f} = f - \overline{f},$$

by averaging along the poloidal y-direction. This modification is shown to induce stronger zonal mean structure[16,18] from direct simulations.

In the BHW model[14], flux correction on the magnetic surfaces is introduced on the flux-balanced vorticity $q^{\mathrm{BHW}} = \nabla^2\varphi - \tilde{n}$ by removing the zonal mean component $\overline{n}$ in the density field. In comparison, the MHW model[11] uses the potential vorticity $q^{\mathrm{MHW}} = \nabla^2\varphi - n$ including the zonal mean density state (see also Eqn. (31) in Section V A). Many physically feasible properties including stronger persistent zonal jets and clear transition in turbulent flux transport are gained through this simple model modification in the BHW model with a detailed study[15–17] on the doubly periodic geometry.

A. The BHW model with channel boundary conditions

The generalized formulation (1) together with the states (2) enables us to apply a more physically feasible *channel domain geometry*, rather than the common doubly periodic boundary condition simply for convenience. By separating the large and small scale components and focus on the dynamics on small scales, the BHW model can be expressed in a similar form as in Refs. 14 and 15

$$\frac{\partial q}{\partial t} + \nabla^\perp\varphi\cdot\nabla q + V\frac{\partial q}{\partial y} - \kappa\frac{\partial\varphi}{\partial y} = \mu\Delta q, \tag{3a}$$

$$\frac{\partial n}{\partial t} + \nabla^\perp\varphi\cdot\nabla n + V\frac{\partial n}{\partial y} + (\kappa - N)\frac{\partial\varphi}{\partial y} = \alpha(\tilde{\varphi} - \tilde{n}) + \mu\Delta n. \tag{3b}$$

The two-dimensional flow is defined on a rectangular channel domain for $\mathbf{x} = (x,y) \in \mathscr{D} = [0, L_x] \times [-L_y, L_y]$. Without loss of generality, we will mostly use the simplified case with $L_x = L_y = L$, while a longer channel case with $L_y > L_x$ will be discussed in Section IV B.

In such a channel domain, the solution is assumed to be periodic along the y poloidal direction agreeing with the poloidal symmetry in the tokamak, while the solid wall boundary condition requires vanishing radial

velocity and fluctuation density field at the channel walls so that $x = 0, L_x$

$$\begin{aligned} q(x,-L_y) &= q(x,L_y), \quad u\,|_{x=0,L_x} = 0, \\ n(x,-L_y) &= n(x,L_y), \quad n\,|_{x=0,L_x} = 0. \end{aligned} \tag{4}$$

The large-scale density structure is already described by a base profile Nx. Thus the disturbance n is set zero along the two boundary walls. The velocity condition for $u = -\partial_y \varphi$ requires constant values for the potential function along the boundaries $\varphi(0,y) = V_0$ and $\varphi(L_x,y) = V_L$. This is equivalent to the introduction of a large-scale profile Vx on top of the disturbance $\varphi\,|_{x=0,L_x} = 0$ by setting $V_0 = 0$ and $V_L = VL_x$ within a shifting constant. The additional large-scale zonal velocity V won't change the solution structure since the model (3) is Galilean invariant to the poloidal boosts[14]. Therefore, we only need to clarify the additional contribution from the base state density N for the generalized model (Section V will give a more detailed explanation for the contributions from N and V). Besides, in the physical models (3), standard viscous boundary layers do not play a significant role since we are mostly interested in the model solutions away from the boundary layer regime.

B. Enstrophy and energy conservation and zonal state equations for the channel flows

For the generalized BHW model (3) in the channel domain, we need to confirm that the general argument for the conservation laws in the doubly periodic domain case[14,18] are still valid with additional caution for the treatment of the radial boundaries at $x = 0, L_x$. The potential enstrophy W and total energy E in the channel domain BHW model can be defined according to the full states ϕ and ρ from equations (1) as

$$W = \frac{1}{2}\int q^2 = \frac{1}{2}\int \left(\nabla^2\phi - \tilde{n}\right)^2, \quad E = \frac{1}{2}\int \left(|\nabla\phi|^2 + \rho^2\right), \tag{5}$$

with the integration over the two-dimensional channel domain $\mathscr{D}$. Notice that the enstrophy W in the BHW model is defined based on the balanced potential vorticity $q = \nabla^2\phi - \tilde{n}$ excluding the zonal mean density $\overline{n}$ contribution, while the total energy E includes both the contributions from the kinetic energy $\frac{1}{2}\int |\mathbf{v}|^2$ and the total density energy $\frac{1}{2}\int \rho^2 = \frac{1}{2}\int (Nx+n)^2$ with the base state zonal density. Through the construction of the balanced model (3), the nonlinear terms from the velocity advection conserve both the total energy and the balanced enstrophy in the same way as in the doubly periodic case. The conservation laws can be also seen from the link with doubly periodic domain case through the odd expansion of the state variables illustrated in the numerical strategy in Section IV.

First, the dynamical equation for the total enstrophy W is determined by the potential vorticity equation (3a). Thus the dynamics is not altered by both the zonal velocity and density profiles V and N. The equation

for the enstrophy can be reached as

$$\frac{dW}{dt} = \kappa \int \overline{\tilde{u}\tilde{n}} - \mu \int |\nabla q|^2 . \tag{6}$$

On the right hand side of the above equation, the total zonal particle flux $\Gamma = \kappa \int \overline{\tilde{u}\tilde{n}}$ acts as a forcing effect to the system. Second, the dynamical equation for the total energy E can be derived in a similar way as

$$\begin{aligned} \frac{dE}{dt} = & \int (\kappa + \overline{v})\, \overline{\tilde{u}\tilde{n}} - \alpha \int (\tilde{n} - \tilde{\varphi})^2 \\ & - \mu \int \left(|\Delta \varphi|^2 + |\nabla n|^2 \right). \end{aligned} \tag{7}$$

The additional term due to the mean velocity $\overline{v} = \partial_x \overline{\varphi}$ advection in the energy equation represents the zonal flow transport of the particle flux, $\overline{\tilde{u}\tilde{n}}$. One negative-definite term due to the resistivity α appears in the equation as an energy sink, while α has no effect on the change of the enstrophy W. In the case without an additional background density gradient N, the energy equation for E gets reduced back to the same form in the doubly periodic domain.

Next, we can also introduce the dynamical equations for the zonal states. The equations for zonal mean states of the potential vorticity $\overline{q}(x) = \partial_x^2 \overline{\varphi}(x)$ and the density $\overline{n}(x)$ in the BHW model after averaging along the periodic y-direction are also not changed on the channel geometry

$$\begin{aligned} \partial_t \overline{q} + \partial_x \left(\overline{\tilde{u}\tilde{q}} \right) &= \mu \partial_x^2 \overline{q}, \\ \partial_t \overline{n} + \partial_x \left(\overline{\tilde{u}\tilde{n}} \right) &= \mu \partial_x^2 \overline{n}. \end{aligned} \tag{8}$$

It needs to be reminded that the first equation above for $\overline{q}$ is not valid in the MHW model case, which leads to the non-conservation of total impulse according to discussions in Section V A. The right hand sides of (8) are due to the collisional viscosity defined by μ. The relation between the eddy vorticity flux $\overline{\tilde{u}\tilde{q}}$ and the particle density flux $\overline{\tilde{u}\tilde{n}}$ can be found using the definitions of $\tilde{u} = -\partial_y \varphi$ and $\tilde{v} = \partial_x \tilde{\varphi}$

$$\overline{\tilde{u}\tilde{q}} = \frac{1}{L_y} \int \tilde{u} \left(\partial_x \tilde{v} - \tilde{n} \right) dy = -\overline{\tilde{u}\tilde{n}} - \partial_x \left(\overline{\tilde{u}\tilde{v}} \right), \tag{9}$$

where the second identity is applied from integration by parts. Especially, the eddy diffusivity as the second term on the right hand side of (9) will vanish after another integration along x. The total fluxes in vorticity and density are related by the same flux strength with opposite signs

$$\int \left(\overline{\tilde{u}\tilde{q}} \right) dx = - \int \left(\overline{\tilde{u}\tilde{n}} \right) dx. \tag{10}$$

C. Large scale density profile from energy conservation

The additional mean density gradient N introduces richer dynamics to the solutions by altering the background density decaying profile. Thus here we discuss more on the contributions from the zonal density state from N. If we just consider the energy in the small-scale density field $E_S = \frac{1}{2}\int\left(|\nabla\varphi|^2 + n^2\right)$ without the large-scale density according to the dynamical equation in (3a) and (3b), the equation for the energy E_S only in small scales implies the following dynamics

$$\begin{aligned}\frac{dE_S}{dt} &= (\kappa - N)\int \tilde{u}\tilde{n} + \int \overline{v}\left(\tilde{u}\tilde{n}\right) \\ &\quad - \alpha\int(\tilde{n}-\tilde{\varphi})^2 - \mu\int\left(|\Delta\varphi|^2 + |\nabla n|^2\right).\end{aligned} \tag{11}$$

Comparing the above equation with the full energy dynamics (7), one additional term related with the large-scale density N appears in the small-scale energy E_S dynamics, which is due to the coupling effect between the two states N and n. By taking the difference of the two energy equations (7) and (11), the dynamical equation reveals the large scale density with an extra coupling term

$$\frac{d}{dt}(E - E_S) = \frac{d}{dt}\left(\frac{N^2}{2}\int x^2 + N\int nx\right) = N\int \tilde{u}\tilde{n}.$$

The cross term between N and n gives a new quantity as the impulse of the density fluctuation, $I_n = \int nx$. In fact, in the formulation of equation (3b), we already assume a constant large-scale density $N(t) \equiv N_0$, that is, $\frac{dN}{dt} = 0$. Therefore, the identity above gives the dynamical equation for the impulse in density

$$\frac{dI_n}{dt} = \frac{d}{dt}\int nx = \int \tilde{u}\tilde{n}.$$

It will be shown next in Section III that the above equation provides a new set of important quantities for the analysis of the channel geometry dynamics.

In addition, the interaction with the linear zonal density profile Nx receives a more reasonable physical interpretation from the BHW model (this structure can be indeed observed in direct channel domain simulations as in Figure 4 from drift instability), while the MHW model cannot generate consistent response from interaction with N. We will give more detailed discussions about the effects from the zonal structure N in Section V.

III. NEW CONSERVED QUANTITIES FOR THE BHW MODEL WITH CHANNEL GEOMETRY

Adopting the channel geometry for the BHW model (3) not only offers a more physically feasible formulation of the plasma edge turbulence[1,2], it also provides a set of additional useful conserved quantities that

helps us to seek a better understanding for the generation of zonal flows and the interaction mechanism with fluctuations. For simplicity in exposition, we adopt the flow fields without the large scale background profiles $V = N = 0$ without loss of generality.

Spectral representation of channel zonal and fluctuation states

The general flow solutions in a channel domain with solid wall boundaries can be linked to the doubly periodic geometry by extending the solution in $x \in [0, L_x]$ to the domain $[-L_x, L_x]$ as an odd function. In this way, the boundary condition, $\varphi\,|_{x=0,L_x} = 0$, $n\,|_{x=0,L_x} = 0$, is automatically satisfied from the odd extension. This trick of odd extension[21] is adopted for computational convenience using the spectral scheme and will be described in Section IV with more details.

For the spectral representation, it is convenient to decompose the states into the zonal mean component $(\overline{\varphi}, \overline{n})$ and the non-zonal fluctuations $(\tilde{\varphi}, \tilde{n})$. First, we can project the non-zonal states on the extended doubly periodic domain under the Fourier modes

$$\tilde{\varphi} = \sum_{k_y \neq 0} \hat{\varphi}_k e^{i\mathbf{k}\cdot\mathbf{x}}, \quad \tilde{n} = \sum_{k_y \neq 0} \hat{n}_k e^{i\mathbf{k}\cdot\mathbf{x}}, \tag{12}$$

where we set the corresponding spectral wavenumber $\mathbf{k} = (k_x, k_y) = \left(\frac{\pi}{L_x} l_x, \frac{\pi}{L_y} l_y\right)$ and $k^2 = |\mathbf{k}|^2$ with increments $\Delta k_x = \pi / L_x, \Delta k_y = \pi / L_y$ and the integer wavenumber indexes $l_x = -\frac{N_x}{2} + 1, \cdots, \frac{N_x}{2}$, and $l_y = -\frac{N_y}{2} + 1, \cdots, \frac{N_y}{2}$. Second, we can propose the expansions of the zonal states $\overline{\varphi}$ and $\overline{n}$ as odd functions

$$\overline{\varphi} = i \sum_{k=k_x} (-1)^l \overline{\varphi}_k e^{ikx}, \; \overline{n} = i \sum_{k=k_x} (-1)^l \overline{n}_k e^{ikx}. \tag{13}$$

The zonal potential vorticity modes can be introduced accordingly as $\overline{q}_k = k^2 (-1)^{l-1} \overline{\varphi}_k$. Above the summation is taken among the zonal modes with $k = k_x = \frac{\pi}{L_x} l_x$ and $k_y = 0$. The decomposition is due to the odd extension of the zonal states to periodic functions so that the coefficients $\overline{\varphi}_{-k} = -\overline{\varphi}_k$, $\overline{n}_{-k} = -\overline{n}_k$ are in real values. The reason for adding the additional coefficients $(-1)^l$ in the zonal modes will become clear when we introduce the spectral forms of the zonal impulses next.

A. Impulse equations for the channel geometry

From the energy equations derived in (11), we already see the emergence of a new quantity induced from the cross interaction between large and small scale zonal density states. In general, the *impulses* for the vorticity I_q

and density I_n can be defined as the first moments of the zonal potential vorticity $\overline{q} = \partial_x^2 \overline{\varphi}$ and the zonal density $\overline{n}$ profiles as

$$I_q = \int_0^L x\overline{q} dx, \quad I_n = \int_0^L x\overline{n} dx. \tag{14}$$

For convenience in the later analysis of showing energy structures in different scales, we express the impulses (14) in terms of the spectral modes (13). In addition, the linear function x in the extended domain $[-L, L]$ as an odd function can be also expanded in Fourier series as

$$x = i \sum_{k=\frac{\pi}{L}l} \frac{(-1)^l}{k} e^{ikx}.$$

Combining the spectral representations of the zonal modes (13), the impulses in (14) can be expanded as a summation of spectral modes in the form

$$I_q = -\sum k\overline{\varphi}_k, \quad I_n = \sum k^{-1}\overline{n}_k. \tag{15}$$

With the alternating signs given in (13), we can write the impulses as the summation of the real spectral coefficients with the same sign in a cleaner representation.

One physical interpretation of the impulse for the vorticity $\overline{q}$ can be found as the *zonal exit velocity* on the right boundary of the channel, that is, from the direct computation of the zonal integration

$$I_q = \int_0^L x\partial_x \overline{v} dx = -\int_0^L \overline{v} dx + x\overline{v} \,|_{x=0}^L = L\overline{v}_R, \tag{16}$$

with $\overline{v}_R(t) \equiv \overline{v}(L,t)$ the velocity along the right boundary. Above the zonal velocity $\overline{v} = \partial_x \overline{\varphi}$ only contains the small scales without the large-scale mean V, thus it gives zero after averaging along x direction. The impulses I_q, I_n are not conserved in time in general. Still, due to the new features from the channel geometry, we are able to discover useful new properties based on the dynamical equations for the impulses that are not available in the doubly periodic domain case.

Next, we derive the dynamical equations for the impulses. The dynamical equations for the impulses of q and n can be derived directly by multiplying x on both sides of the zonal mean equations (8) and then taking integration along x. The final dynamical equations for the impulses can be found as

$$\begin{aligned} \frac{dI_q}{dt} &= \int_0^L \left(\overline{\tilde{u}\tilde{q}}\right) dx + \mu \partial_x \overline{q}_R, \\ \frac{dI_n}{dt} &= \int_0^L \left(\overline{\tilde{u}\tilde{n}}\right) dx + \mu \partial_x \overline{n}_R. \end{aligned} \tag{17}$$

The last terms on the right hand sides add the collisional effects from the viscosity μ, and they are only related with the zonal values $\overline{q}_R \equiv \overline{q}(L,t), \overline{n}_R \equiv \overline{n}(L,t)$ evaluated at $x = L$. For the impulse of the vorticity, we have

$\mu\partial_x\overline{q}_R = \mu\partial_x^2 I_q$. In the derivation of the above equations, we again apply the non-penetrating channel wall boundary condition (4) for vanishing velocity $\tilde{u}\,|_{x=0,L}= 0$ at the channel boundaries $x = 0, L$ such that

$$-\int_0^L x\partial_x\left(\overline{\tilde{u}\tilde{f}}\right) = \int_0^L \overline{\tilde{u}\tilde{f}} - x\left(\overline{\tilde{u}\tilde{f}}\right)\,|_{x=0}^{L} = \int_0^L \left(\overline{\tilde{u}\tilde{f}}\right) dx.$$

The dynamical equations for the impulses (14) offer an additional link between the zonal states and the total particle flux seen in the energy/enstrophy equations (6) and (7). In particular from the relation in (10), $\int \overline{\tilde{u}\tilde{q}} = -\int \overline{\tilde{u}\tilde{n}}$, the right hand sides for I_q and I_n dynamics get cancelled due to the same flux with opposite signs. Using the spectral representation (13), we can write the dynamical equation for the combined impulses as

$$\frac{d}{dt}\sum k^{-1}\left(\overline{n}_k - k^2\overline{\varphi}_k\right) = -\mu\sum k\left(\overline{n}_k - k^2\overline{\varphi}_k\right). \tag{18}$$

The right hand side of the above equation is purely from the dissipation effect, and the total impulse $I = I_q + I_n$ becomes conserved in time in the inviscid flow $\mu = 0$.

Remark. The above arguments are still valid with the inclusion of a background density and velocity profiles N and V. We just need to replace the density field n by the original full density $\rho = Nx + n$, then all the above results remain true for the impulses defined by the full density $I_\rho = \int x\rho$. Therefore, the same conclusion can be reached with no further modification on the equations.

B. New conserved quantities and bounds in the zonal mean and fluctuation states

In this section for the discussion of the new conserved quantities, we neglect the dissipative effect from the collisional terms $\mu \equiv 0$ to focus on the mechanisms in the linear and nonlinear interactions. The driving term on the right hand sides of the impulse equations (17) represents the total fluxes (in vorticity and density) along the radial direction, with zero transport across the channel walls. Using the relation for the total fluxes for the vorticity and density (10), the impulse equations for the channel domain can be linked as

$$\frac{dI_q}{dt} = \int \overline{\tilde{u}\tilde{q}} = -\int \overline{\tilde{u}\tilde{n}} = -\frac{dI_n}{dt}. \tag{19}$$

Therefore, we have the first conserved constant depending on the zonal states as the total impulse combining the first moments of potential vorticity and particle density

$$\frac{dI}{dt} = 0, \quad I = I_q + I_n = \int_0^L x\left(\overline{q} + \overline{n}\right) dx, \tag{20}$$

in the inviscid dynamics. Especially, if we assume that the flow starts from zero zonal states $\overline{q} = \overline{n} = 0$ at initial time $t = 0$, the conservation of total impulse I guarantees the identity in the two impulses $I_q = -I_n$ during the

entire evolution time. From the equation for the impulses (17), usually a strong total particle flux $\int \tilde{u}\tilde{n} > 0$ will be induced at the starting transient state due to drift instability (see the numerical simulations in Section IV for a direct confirmation). This leads to a negative vorticity impulse $I_q < 0$ and a positive density impulse $I_n > 0$ in the final steady state.

As a further comment according to the expression for the vorticity impulse (16), introducing the zonal exit velocity $\overline{v}_R(t)$ on the right boundary of the channel, we have the link between the zonal velocity and the total particle flux from

$$\frac{d}{dt}\overline{v}_R = -\frac{1}{L}\int \overline{\tilde{u}\tilde{n}}.$$

The above equation implies that a strong positive particle flux will generate a negative zonal exit velocity $\overline{v}_R < 0$ along the y direction in the final steady state (this is also confirmed in the numerical results in Figure 4 for the zonal profiles). The dynamics for the impulses provide an important link between the fluctuating particle flux from non-zonal modes and the zonal state profile. This enables us to construct conserved quantities in combination with the energy and enstrophy equations.

1. Effective bounds from the enstrophy and impulse equations

The impulse dynamics (19) links the zonal states with the total particle flux transport. This equation can be first combined with the total enstrophy equation (6) for W, which is only driven by the total particle flux with the parameter κ in the inviscid case. Adding the dynamical equations for the impulses and the total enstrophy, we find a conserved quantity for the inviscid channel BHW model where the total particle flux in the two equations cancels with each other

$$\frac{d}{dt}\left(W + \kappa I_q\right) = 0, \quad W + \kappa I_q = W - \kappa I_n, \tag{21}$$

using the identity between the impulses $I_n = -I_q$. The above conservation law offers a useful relation for the balance between the fluctuation modes (represented by the enstrophy fluctuation $\tilde{W}$) and the zonal state (represented by the impulse I and zonal part $\overline{W}$).

The conservation relation in (21) enables us to discover the maximum growth in the zonal states and the total increase in the non-zonal fluctuation modes from the initial state. A common setup for simulations of the model (3) is to start with a small non-zero fluctuation state $\tilde{q}_0$ with zero zonal state at the initial time. The non-zonal drift waves first rise up due to the linear instability in the fluctuation modes in the starting transition stage; then the zonal modes are excited through nonlinear interactions from secondary instability. The energy

transfer mechanism is discussed in detail in Refs. 16 and 17. Here with the new conserved quantity, we aim to explore the saturated growth in the zonal state and fluctuation modes as the model parameter varies.

The conservation relates the states at the initial time $t = 0$ and a later stage at time t

$$W(t) - \kappa I_n(t) = \tilde{W}_0,$$

assuming the initial total enstrophy $\tilde{W}_0 = W(0) - \kappa I_n(0) \ll 1$ in a small value containing only non-zonal fluctuation modes. We decompose the total enstrophy W defined in (5) into the zonal and non-zonal components to clarify the contribution from each part

$$\overline{W} = \frac{1}{2}\sum_{k=k_x} k^4 \overline{\varphi}_k^2, \quad \tilde{W} = \frac{1}{2}\sum_{k_y\neq 0} \left|k^2\tilde{\varphi}_k + \tilde{n}_k\right|^2,$$

where we adopt the spectral representation of the non-zonal modes $\mathbf{k} = (k_x, k_y)$, $k_y \neq 0$ in (12) and the zonal $\mathbf{k} = (k_x, 0)$ in (13). Separating the total zonal state and the fluctuation enstrophy growth due to instability, we have the relation between the zonal states and the increase in the total fluctuations in enstrophy

$$\kappa I_n - \overline{W} = \tilde{W}(t) - \tilde{W}_0 = \frac{1}{2}\int \left(\tilde{q}^2 - \tilde{q}_0^2\right).$$

with $\tilde{q} = \nabla^2\tilde{\varphi} - \tilde{n}$ the non-zero potential vorticity in fluctuation. Equivalently, we can express the above relation as a summation of the spectral modes for different scales

$$\begin{aligned}\sum_{k=k_x}\left(\kappa k\overline{\varphi}_k - \frac{1}{2}k^4\overline{\varphi}_k^2\right) &= \sum_{k=k_x}\left(\kappa k^{-1}\overline{n}_k - \frac{1}{2}k^4\overline{\varphi}_k^2\right)\\ &= \frac{1}{2}\sum_{k_y\neq 0}\left(|\tilde{q}_k|^2 - \left|\tilde{q}_{0,k}\right|^2\right) > 0\end{aligned} \tag{22}$$

Above the explicit expressions for the impulses (15) are used. The lower row of the above identity should be positive for drift instability to excite turbulent waves from the small initial state $\tilde{W}_0$. The above equality shows that the total variability among all the fluctuation modes can be determined by the zonal mean modes only along the x direction.

First, we consider the maximum growth in the non-zonal fluctuations. From the left side of equation (22) for the summation among all zonal modes $\overline{\varphi}_k$, it forms a quadratic form for each wavenumber k_x. Each quadratic function has an upper bound, $\kappa k u - \frac{k^4}{2}u^2 \leq \frac{\kappa^2}{2k^2}$ among all values of u. Thus we find the maximum growth for the enstrophy in non-zonal fluctuations averaged over the computational domain area $A = L_x L_y$

$$\frac{1}{A}\int\left(\tilde{q}^2 - \tilde{q}_0^2\right) \leq \frac{\kappa^2}{L_x L_y}\sum_{k=k_x} k^{-2} \leq \frac{L_x}{3L_y}\kappa^2. \tag{23}$$

The last inequality above uses the formula for the summation of reciprocals of the squares of the natural numbers l with $k_x = \frac{\pi}{L_x} l$. The bound (23) estimates the saturated growth in total enstrophy fluctuation after the first linear instability and then the secondary transfer of energy to zonal modes. The bound can be even tighter considering that there is usually limited number of dominant zonal modes in the largest scales. It is important to observe that a long channel width L_x will generate stronger fluctuations as well as a stronger background density gradient κ, while a longer channel length L_y will reduce the averaged total fluctuations in the system.

Next, from the other direction, the positiveness of the second row of the above equality (22) for increasing fluctuations provides a necessary condition for at least one positive contribution from the zonal modes in the first row. If the zonal solution converges to a dominant critical zonal state with a single wavenumber k_c, the single mode solution in the zonal state must obey the following constraints to maintain the positiveness

$$0 < \overline{\varphi}_{k_c} < \frac{\kappa}{k_c^3}, \quad \overline{v}_{k_c}^2 < \frac{2\kappa}{k_c^3} \overline{n}_{k_c}, \tag{24}$$

with the energy in the zonal velocity $\overline{v}_k^2 = k^2 \overline{\varphi}_k^2$. The above bounds offer constraints for the dominant steady state zonal amplitudes. The bounds for enstrophy achieved here are independent of the adiabaticity parameter α.

2. Slaving relation between small and large scales from energy and impulse equations

We can also seek the corresponding relation from the combination with the total energy equation (7). It shows from the total energy dynamics that the adiabaticity parameter α keeps reducing the total energy through the interacting fluctuation modes. Applying the same strategy as before, the total particle flux on the energy dynamics can be again canceled by the impulse equation so that

$$\frac{d}{dt}\left(E + \kappa I_q\right) = \frac{d}{dt}\left(E - W\right) = \int \overline{v}\left(\overline{\tilde{u}\tilde{n}}\right) - \alpha \int \left(\tilde{n} - \tilde{\varphi}\right)^2, \tag{25}$$

for the inviscid system. The first equality above uses the conservation of $W + \kappa I_q$. A conservation law cannot be reached from the energy equation due to both the resistive term from α and the contribution from the zonal flow advection $\overline{v}$ appearing on the right hand side of (25). To find estimation using the energy constraint, we need to adopt additional arguments based on observations in the solutions. In the starting transient state, the nonlinear coupling term, $\int \overline{v}\left(\overline{\tilde{u}\tilde{n}}\right)$, is often dominant and injects energy into the entire spectrum. On the other hand, if we look at the long time performance as $t \to \infty$, the negative definite resistive term at the right hand side of (25) will take the dominant role while the zonal flow and particle flux will converge to the steady state with

a much smaller value in the first coupling term (This argument can be verified from the direction numerical simulations shown in Figure 2).

In this case after long enough time $t \gg 1$, we can assume that the right hand side of (21) becomes negative. Then the difference $E(t) - W(t) \geq E_\infty - W_\infty$ is decreasing to the final limiting value. Further, if we assume that the final limiting state always stays positive, $E_\infty - W_\infty > 0$ (this can again be confirmed from numerical simulations shown next in Figure 2). The difference between the energy and enstrophy can be rearranged into the spectral modes as

$$\begin{aligned} E - W &= \sum k^2 |\hat{\varphi}_k|^2 + |\hat{n}_k|^2 - \left|k^2 \hat{\varphi}_k + \hat{n}_k\right|^2 \\ &= \sum k^2 \left(1 - k^2\right) |\hat{\varphi}_k|^2 - 2k^2 \hat{\varphi}_k \cdot \hat{n}_k > 0, \end{aligned}$$

where both the zonal state and fluctuation modes are included. The coefficients above can be divided into two groups according to the sign of the wavenumber k^2. Therefore a slaving relation is found between the energy $E_k = k^2 |\hat{\varphi}_k|^2 + |\hat{n}_k|^2$ and enstrophy $W_k = \left|k^2 \hat{\varphi}_k + \hat{n}_k\right|^2$ in large and small scales

$$\begin{aligned} \sum_{k^2<1} E_k &\geq \sum_{k^2<1} k^2 \left(1 - k^2\right) |\hat{\varphi}_k|^2 - 2k^2 \hat{\varphi}_k \cdot \hat{n}_k \\ &> \sum_{k^2>1} \left(W_k - E_k\right). \end{aligned} \tag{26}$$

The first inequality above is applied for modes in larger scales $k^2 < 1$, thus we use the additional estimation with the help of the triangular inequality, $2k^2 |\hat{\varphi}_k \cdot \hat{n}_k| \leq k^4 |\hat{\varphi}_k|^2 + |\hat{n}_k|^2$. For the modes in smaller scales $k^2 > 1$, it is safe to assume that the non-zonal fluctuation modes dominate and the contribution from the zonal modes are negligible. Notice that the energy E_k is usually smaller than the enstrophy W_k in small scale modes so the difference stays positive. The bound in (26) offers us one slaving relation between the modes in small and large scales. The left hand side contains only a small number of large scale modes. It controls the total variability of all the small scale modes over a wide spectrum from the summation on the right hand side. The relation in (26) provides a useful reference for the maximum total fluctuations in the large number of small-scale modes.

We summarize the conclusions in the following proposition:

Proposition 1. *The impulse functions combined with the enstrophy and energy provide the bounds for the total variability in the BHW model solutions:*

- *The maximum saturated growth in total fluctuations and the dominant zonal mode from small initial state can be estimated by (23) and (24) using the enstrophy and impulse equations;*

- *The long time performance for the competition between the energy in largest scales in $k < 1$ and small*

scale fluctuations in wavenumbers $k > 1$ can be estimated by the slaving relation (26) using the energy and impulse equations.

C. Balance in statistical steady state with non-zero collisional viscosity

The previous discussions concern the competition between zonal states and fluctuations from instability with the help of the new conserved quantities, while no viscosity effect is included. In this final part, we seek the statistical variability in the final equilibrium steady state, which requires the balance between the turbulent fluxes and the collisional viscosity as a dissipation effect in the statistical steady state. More detailed constraints for the variances in the zonal mean and fluctuation states can be found.

Instead of the performance of one single solution, the statistics characterize the ensemble mean and variance in the group performance of solutions[22]. So we introduce the statistical average operator $\langle\cdot\rangle$ for the long time/ensemble average of the solutions. The idea here is to consider the statistical equations for the enstrophy or energy together with the impulses. First, exploiting the impulse equations in statistical steady state, the ensemble averaged $\langle I_n\rangle$ and $\langle I_q\rangle$ become constants. The right hand sides of the dynamical equations (17) together with the spectral representation of the zonal mean modes (13) give the equality in statistical steady state

$$\langle\Gamma\rangle = \mu\sum k\langle\overline{n}_k\rangle = \mu\sum k^3\langle\overline{\varphi}_k\rangle\,, \tag{27}$$

where the equilibrium statistical particle flux can be found as $\langle\Gamma\rangle = \int_0^L \langle\overline{\tilde{u}\tilde{n}}\rangle\, dx$. The above equality also offers a direct relation in the statistical mean states of the zonal density and potential modes

$$\sum k\left(\langle\overline{n}_k\rangle - k^2\langle\overline{\varphi}_k\rangle\right) = 0.$$

In particular, if we assume that the statistical mean spectra of the zonal density and velocity field follow the power laws, $|\langle\overline{n}_k\rangle|^2 \sim k^{-a}$ and $|\langle\overline{v}_k\rangle|^2 \sim k^{-b}$, the above identity implies the relation, $b-a=2$, between the exponents in density and kinetic energy spectra.

Next, we consider the statistical steady state in the enstrophy equation (6). The balance between the particle fluxes and the dissipations at statistical equilibrium gives

$$\kappa\langle\Gamma\rangle = \frac{\mu}{2}\sum_{k\neq k_y} k^2\left\langle\left|k^2\tilde{\varphi}_k + \tilde{n}_k\right|^2\right\rangle + \frac{\mu}{2}\sum_{k=k_x} k^6\langle\overline{\varphi}_k^2\rangle\,.$$

Above on the right hand side, we separate the contributions from the zonal state and the fluctuation modes with $k_y \neq 0$. Combining the above relation with the previous equality from the statistical impulses (27), we find the

balance between the statistics in mean states and the total variance about the mean

$$\sum\left(\kappa k^3\left\langle\overline{\varphi}_k\right\rangle-\frac{k^6}{2}\left\langle\overline{\varphi}_k\right\rangle^2\right)=\frac{1}{2}\sum k^2\mathrm{var}\left(\tilde{q}_k\right)+k^2\mathrm{var}\left(\overline{q}_k\right).$$

Above we separate the statistical average of the quadratic variables into the statistical mean and variance as $\left\langle f^2\right\rangle=\left\langle f\right\rangle^2+\mathrm{var}\left(f\right)$. The right hand side of the above equality gives the variances in the zonal vorticity, $\mathrm{var}\left(\overline{q}_k\right)=\left\langle\left(\overline{q}_k-\left\langle\overline{q}_k\right\rangle\right)^2\right\rangle$, and in the fluctuations, $\mathrm{var}\left(\tilde{q}_k\right)=\left\langle\left|k^2\tilde{\varphi}_k+\tilde{n}_k\right|^2\right\rangle$. The left hand side only includes the statistical mean of the zonal steady state $\left\langle\overline{\varphi}_k\right\rangle$. Thus we can compute the upper bound for the total variance in statistical equilibrium enstrophy

$$\frac{1}{2}\sum k^2W_k^{\mathrm{var}}\leq\sum k^3\left(\kappa\left\langle\overline{\varphi}_k\right\rangle-\frac{k^3}{2}\left\langle\overline{\varphi}_k\right\rangle^2\right)\leq\sum\frac{\kappa^2}{2}=\frac{C}{2}\kappa^2. \tag{28}$$

The last inequality above uses the upper bound for the quadratic form for each wavenumber, and C is a constant from the effective number of the non-zero zonal modes. The above inequality offers an estimate for the maximum total variance among all the enstrophy modes $W_k^{\mathrm{var}}=\mathrm{var}\left(\tilde{q}_k\right)+\mathrm{var}\left(\overline{q}_k\right)$ depending only on the model parameter κ.

Finally, we consider the statistical equilibrium state from the energy equation (7) together with the impulse

$$\kappa\left\langle\Gamma\right\rangle\geq\alpha\sum\left\langle\left|\tilde{n}_k-\tilde{\varphi}_k\right|^2\right\rangle+\frac{\mu}{2}\sum\left(k^4\left\langle\left|\tilde{\varphi}_k\right|^2\right\rangle+k^2\left\langle\left|\tilde{n}_k\right|^2\right\rangle\right)+\frac{\mu}{2}\sum\left(k^4\left\langle\overline{\varphi}_k^2\right\rangle+k^2\left\langle\overline{n}_k^2\right\rangle\right).$$

The important approximation used above is to assume that the advected flux is non-positive at statistical equilibrium, $\int\left\langle\overline{v}\left(\overline{\tilde{u}\tilde{n}}\right)\right\rangle\leq 0$ (this is from observations in the computational results shown next in Figure 2). Again using the statistical balances in the impulses (27) to replace the total particle flux $\left\langle\Gamma\right\rangle$ on the left, we find the relation between the mean and variance in statistical steady state

$$\begin{array}{c}\frac{1}{2}\sum k\left(\kappa\left\langle\overline{n}_k\right\rangle-k\left\langle\overline{n}_k\right\rangle^2\right)\\ \frac{1}{2}\sum k^3\left(\kappa\left\langle\overline{\varphi}_k\right\rangle-k\left\langle\overline{\varphi}_k\right\rangle^2\right)\end{array}\geq\frac{\alpha}{\mu}\sum\mathrm{var}\left(\tilde{n}_k-\tilde{\varphi}_k\right)+\begin{array}{c}\frac{1}{2}\sum k^2\mathrm{var}\left(n_k\right)\\ \frac{1}{2}\sum k^2\mathrm{var}\left(v_k\right)\end{array},$$

with $|v_k|=k\left|\varphi_k\right|$. We summarize the statistics among mean on the left hand side, while the variances on the right. Applying the same trick as before using the positiveness of the right hand side above, the above inequality can be further organized into the balance between the mean and variance according to the statistical energy

$$\begin{aligned}&\sum k^2E_k^{\mathrm{var}}+\frac{\alpha}{\mu}\sum\mathrm{var}\left(\tilde{n}_k-\tilde{\varphi}_k\right)\\ \leq&\frac{1}{2}\sum k\left(\kappa\left\langle\overline{n}_k\right\rangle-k\left\langle\overline{n}_k\right\rangle^2\right)+\frac{1}{2}\sum k^3\left(\kappa\left\langle\overline{\varphi}_k\right\rangle-k\left\langle\overline{\varphi}_k\right\rangle^2\right)\\ \leq&\sum\left(1+k^2\right)\frac{\kappa^2}{8}=\frac{C'}{8}\kappa^2.\end{aligned} \tag{29}$$

where $E_k^{\text{var}} = \text{var}(v_k) + \text{var}(n_k)$ measures the variance in the total energy, and $\text{var}(\tilde{n}_k - \tilde{\varphi}_k)$ is the variance in the deviation from the one-field Hasegawa-Mima state at $\alpha = \infty$[23,24]. The above bound is useful to show the role of a dominant zonal state to quench the energy in fluctuations. A weak zonal mean profile, $\langle \overline{n}_k \rangle, \langle \overline{\varphi}_k \rangle < \frac{\kappa}{2k}$, reduces the upper bound amplitude on the right hand side. Thus the total variance in the fluctuation modes is constrained in small values.

The above conclusions for the total variance in the statistical steady state solutions can be summarized in the following proposition:

Proposition 2. *By comparing the balance between the total particle flux and the dissipation effect, the total variance in statistical solutions of the BHW model can be estimated as:*

- *The statistical impulse equations predict the steady state mean spectra in the relation (27) with slopes in the inertia range* $|\langle \overline{n}_k \rangle|^2 \sim k^{-a}$ *and* $|\langle \overline{v}_k \rangle|^2 \sim k^{-b}$ *and* $b - a = 2$*;*
- *The statistical enstrophy and impulse equations give the bound for total variance in enstrophy controlled by the zonal statistical mean state as in (28);*
- *The statistical energy and impulse equations estimate the total variance in energy from the zonal statistical mean states as in (29).*

IV. NUMERICAL ILLUSTRATION FOR THE BHW FLOWS IN THE CHANNEL DOMAIN

In this section, we carry out direction numerical simulations to illustrate the typical flow structures in the channel domain and to confirm the theoretical bounds derived using the new conserved quantities. For efficient numerical computation, an additional trick should be adopted to generalize the pseudo spectral scheme for the doubly periodic domain case used in Ref. 15. To ensure the geometry for the channel domain, we set the boundary values for both φ and n as in (4)

$$\begin{aligned} \varphi(0,y,t) =& \varphi(L_x,y,t) = 0, \\ n(0,y,t) =& n(L_x,y,t) = 0. \end{aligned} \tag{30}$$

With the above vanishing boundary values for the states, the channel domain solution can be extended to the doubly periodic domain on $[-L_x, L_x] \times [-L_y, L_y]$ with an odd extension along the x direction so that

$$\tilde{f}(x,y) = \begin{cases} f(x,y), & 0 \le x \le L_x, \\ -f(-x,y), & -L_x \le x < 0. \end{cases}$$

This new function $\tilde{f}$ becomes doubly periodic and naturally satisfies the channel boundary condition (30) on the constrained regime $[0, L_x] \times [-L_y, L_y]$. In practice, $\tilde{f}$ can be computed by applying Fourier expansion in y direction and sine expansion in x direction. In this way, the new solution can be exactly summarized into the original double periodic framework with the corresponding constraints on spectral modes as shown in (12) and (13) for fluctuation and zonal modes. In the computational setup for the simulations, the initial state is taken from a random field with small fluctuations. The computation domain is set with equal size in the two directions $L_x = L_y = 20$ except the last case with a long channel $L_y = 100$. Besides, a hyperviscosity, $-\nu\Delta^s q$ and $-\nu\Delta^s n$, is added to the smallest scales of the potential vorticity and density fields with a tiny coefficient $\nu = 7 \times 10^{-21}$ and a high dissipation order $s = 8$ in both the inviscid and dissipative cases in general to dissipate the additional energy in the underresolved smallest scales (but with little impact on the theoretical bounds).

A. Confirmation of the theoretical bounds from direct simulations

1. Bounds for inviscid channel flows with different values of κ

In the first test case, we consider the inviscid channel flows with zero dissipation $\mu = 0$. This enables us to focus on the nonlinear interactions in the dynamics and confirm the bounds for the zonal state and fluctuation growth derived in Section III B from the new conserved quantities. In Figure 1, we compute the saturated values of the dominant zonal mode and the total increase in the enstrophy fluctuation from the small initial state with different values of κ. The zonally averaged profiles of the electrostatic potential $\overline{\varphi}_k$ and the ratio $\overline{n}_k/\overline{\varphi}_k^2$ are dominated by a single wavenumber mode k_c, in agreement with the assumption in the theoretical analysis. The saturation bounds with enstrophy and impulse in (24) predict the upper limit proportional to κ for potential function $\overline{\varphi}_k$, and lower limit inversely proportional to κ for the ratio $\overline{n}_k/\overline{\varphi}_k^2$. The same relations are recovered from the direct numerical results in the left and middle panel of Figure 1. Accordingly, the saturated growth in the total enstrophy fluctuation is also verified in the direct numerical results agreeing with the trend proportional to κ^2 from the theoretical estimation (23). Especially, the bounds for both the zonal mean state and fluctuations become very tight as the system approaches the turbulent regime with large values of κ.

The typical flow solution from direct numerical simulations of the BHW model is then displayed. Figure 2 plots the energetics from a representative flow solution in the turbulent regime with $\alpha = 0.5$ and $\kappa = 1$. In the time-series for the total enstrophy, frequent impulses can be observed as the intermittent injection of energy to the system. The enstrophy in zonal state (in dashed lines) arises at a later time from the secondary transition of the excited turbulent drift waves. Starting from tiny initial condition, the energy and enstrophy

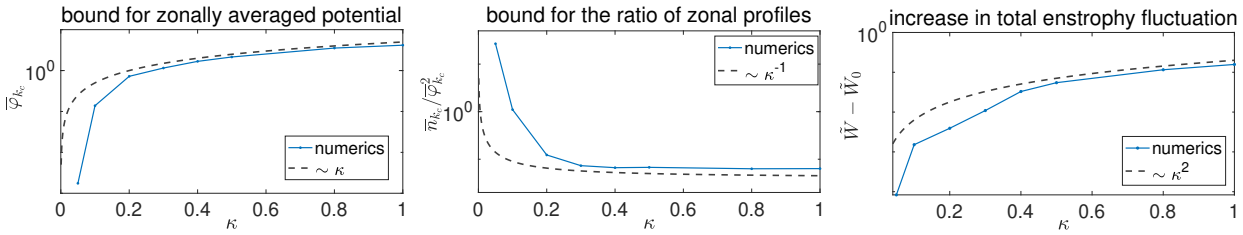

FIG. 1. Changes in the final zonal state $\overline{\varphi}_k$ (left) and the ratio $\overline{n}_k/\overline{\varphi}_k^2$ (middle) at the largest dominant single wavenumber k_c, and the increase in the total enstrophy fluctuation $\tilde{W}-\tilde{W}_0$ (right) with different values of κ and fixed $\alpha=0.5$ in the BHW model simulations. The bounds for the total fluctuations and the zonal mean profiles with dependence on κ computed by (23) and (24) are compared in dashed lines.

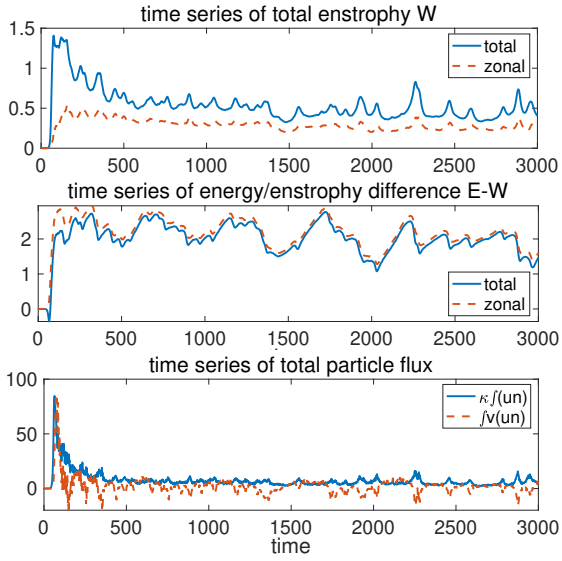

FIG. 2. Time-series of flow energetics from direct numerical simulation with the model parameters $\kappa=1,\alpha=0.5$. The first two rows plot the time evolutions of the total enstrophy W and the difference of energy and enstrophy $E-W$ in total and in zonal modes. The last row compares the evolution of total particle flux $\kappa\int\overline{\tilde{u}\tilde{n}}$ and the advected flux $\int\overline{v}\left(\overline{\tilde{u}\tilde{n}}\right)$ appearing in the full energy equation (7).

difference $E-W$ develops to positive values in the final steady state consistent with our assumption in the analysis for the energy equation (25). Further, we compare the time evolution of the total particle flux $\kappa\int\overline{\tilde{u}\tilde{n}}$ and the advected flux $\int\overline{v}\left(\overline{\tilde{u}\tilde{n}}\right)$, which have a combined effect in the dynamical equation for the total energy (7). Again in agreement with our previous assumption for the analysis, the particle flux $\kappa\int\overline{\tilde{u}\tilde{n}}$ gives intermittent positive excitations, while the advected flux $\int\overline{v}\left(\overline{\tilde{u}\tilde{n}}\right)$ generates negative values in the long time performance after a large positive burst in the starting transient stage.

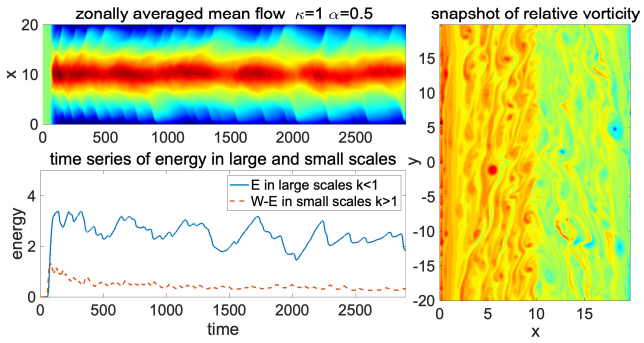

FIG. 3. Time-series of the zonal mean flow $\bar{v}$ and the energy in small and large scale modes (left), and a snapshot of the flow vorticity field (right) with model parameters $\kappa = 1, \alpha = 0.5$.

To illustrate the flow field structure, we also plot the time evolutions of the zonal velocity $\bar{v}$ and the energy contained in small and large scale modes in Figure 3. The evolution of the zonal flow $\bar{v}$ displays strong and rapid variations and shifts in time showing the highly unsteady feature in the zonal states. The energy in both small and large scales shoots up in the starting state from the drift instability and nonlinear energy exchanges. The small scale fluctuations $\sum_k (W_k - E_k)$ in modes $k > 1$ is bounded from above by the limited number of large-scale energy $\sum_k E_k$ in modes $k < 1$. This confirms the slaving relation we found in (26) based on the energy and impulse equations. Finally, the right panel of Figure 3 shows a typical snapshot of the flow ion vorticity field. In the channel domain case, the flow is organized into a dominant large-scale zonal structure with the many interacting small-scale fluctuating vortices coexisting in the field for all the time.

2. *Channel flows with dissipation effect*

Next, we check the statistical balance in the final flow solutions with non-zero dissipation. In this case, a small viscosity $\mu = 1 \times 10^{-4}$ is added in both the potential vorticity and density equations (3). The statistical mean and variance for the interested variables are computed by long time averaging along the steady state trajectory, that is, $\langle f \rangle = \frac{1}{T} \int_t^{t+T} f(s)\, ds$. We also separate the statistics in the mean $\langle f \rangle$ and the variance $\left\langle |f - \langle f \rangle|^2 \right\rangle$ to give a clear comparison.

In Figure 4, we show the statistical mean profile in the zonal state, and the energy spectra for the variance with different values of κ. It is observed that the non-zero statistical mean concentrates on one single zonal wavenumber while all the non-zonal fluctuation modes have the mean near zero. A dominant single jet emerges as the flow becomes more turbulent with larger values of κ. The mean zonal density state shows a nearly linear decay profile. This validates from direct numerical results the proposed zonal structure in the model (2) for a

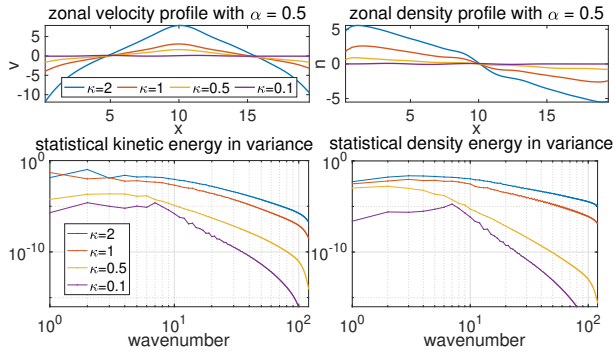

FIG. 4. Zonal state profiles (upper) of the velocity $\overline{v}$ and density $\overline{n}$ and energy spectra in variance (lower) of the kinetic energy var(v_k) and the density energy var(n_k) with different values of κ and $\alpha = 0.5$.

linear large-scale zonal density profile Nx. In the variance, energy spectra for variance in each scale are also compared with various values of κ. Again we observe the rapid transition to turbulent flows with large variance as the value of κ increases. Especially, the largest variance usually occurs among the largest scales representing the fluctuating zonal jet shown in Figure 3.

Then, we can also check the statistical variance bound derived in Section III C. First according to the statistical balance in impulses (27), the energy spectra in statistical mean states should satisfy the inertia slopes $|\langle\overline{n}_k\rangle|^2 \sim k^{-a}$ and $|\langle\overline{v}_k\rangle|^2 \sim k^{-b}$ with difference $b-a=2$. Figure 5 compares the spectra of the statistical mean in two regimes with strong turbulent flow $\kappa = 1$ and with weak turbulence $\kappa = 0.1$. In both cases, the kinetic energy and density energy in mean states follow the difference of powers with a factor of 2 in the inertia range. On the other hand, the mean state in the weak turbulence case $\kappa = 0.1$ decays much faster in smaller amplitudes than the turbulent case $\kappa = 1$. The total variance in enstrophy according to the bound (28) with changing values of κ is also confirmed. The total variances from direct numerical simulations are consistent with the predicted growth in the trend κ^2 as κ grows to the turbulent regime in large values.

Heuristic results from statistical mean state spectra

In the growth in total variance in Figure 5, one additional observation is a phase transition as the value of κ increases. For $\kappa < 1$, the total variance stays in a small value and grows slowly where nearly no turbulence is generated; then after $\kappa > 1$, the total variance jumps to a much higher value and grows in a faster rate. This should be related with the 'Dimits shift' that has been investigated among many other models[19,20].

Here we can also provide one characterization for this transition using the statistical bound derived in (28)

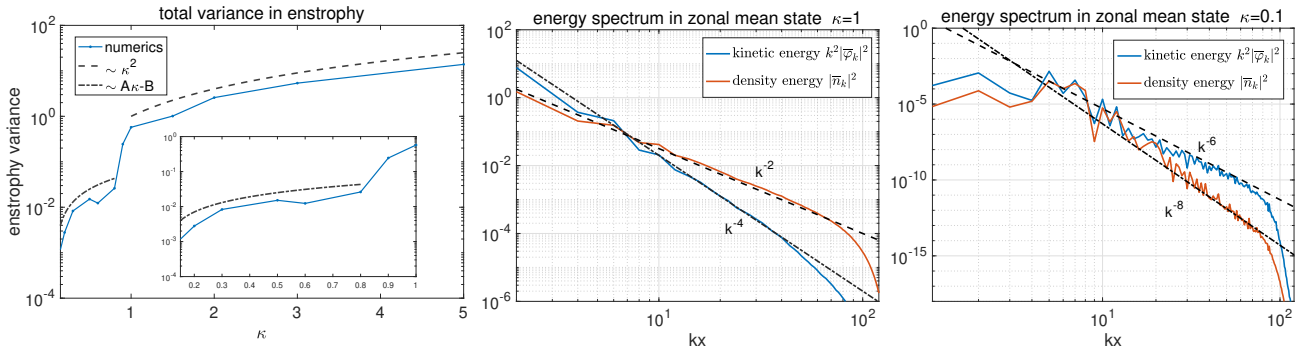

FIG. 5. Total variance in enstrophy according to the bound in (28) with changing values of κ; and energy spectra of the statistical mean in zonal modes in two parameter regimes $\kappa = 1$ and $\kappa = 0.1$.

for the total variance and the zonal mean structure. Notice that the upper bound in (28) for the total variance assumes a maximum contribution in the zonal mean state summation for all scales

$$\frac{1}{2}\sum k^2 W_k^{\text{var}} \simeq \sum k^3 \left(\kappa \langle \overline{\varphi}_k \rangle - \frac{k^3}{2} \langle \overline{\varphi}_k \rangle^2 \right) \sim \sum \max_u k^3 \left(\kappa u - \frac{k^3}{2} u^2 \right) \sim \kappa^2.$$

For this upper bound to be reached, the dominant zonal mean state in the largest scales is required to stay near the critical value to give the maximum value, that is, $\langle \overline{\varphi}_k \rangle \sim k^{-3}\kappa$. This relation is exactly guaranteed in the turbulent regime with $\kappa = 1$ as shown in the middle panel of Figure 5, that is, $\langle \overline{v}_k^2 \rangle = k^2 \langle \overline{\varphi}_k^2 \rangle \sim k^{-4}$ from the largest scale all the way to small scales until the hyperviscosity takes over. Therefore the growth trend $\sim \kappa^2$ is expected in the turbulent regime with large $\kappa \geq 1$. On the other hand for smaller values of κ, the zonal mean state $\langle \overline{\varphi}_k \rangle$ is in much weaker amplitude as shown in the $\kappa = 0.1$ case in the right panel of Figure 5. In this case, the largest scale zonal modes in much smaller values can no longer provide a dominant contribution to guarantee the κ^2 growth. Instead, if we adopt the $\kappa = 0.1$ case, the inertia range gives the slope $\langle \overline{v}_k^2 \rangle = k^2 \langle \overline{\varphi}_k^2 \rangle \sim k^{-8}$, thus $\langle \overline{\varphi}_k \rangle \sim k^{-5}$. Thus the estimation gives the upper bound in smaller amplitude with major contribution from smaller scale inertia modes

$$\frac{1}{2}\sum k^2 W_k^{\text{var}} \leq \sum k^3 \left(\kappa \langle \overline{\varphi}_k \rangle - \frac{k^3}{2} \langle \overline{\varphi}_k \rangle^2 \right) \sim \sum \left(\kappa k^{-2} - \frac{k^{-4}}{2} \right) = A\kappa - B.$$

Therefore, the total variance in the less turbulent regime generates growth in a much slower rate proportional to κ and in a much smaller value. This can also be observed qualitatively in the simulations as in the expanded plot in left panel of Figure 5 for the small value regime of κ.

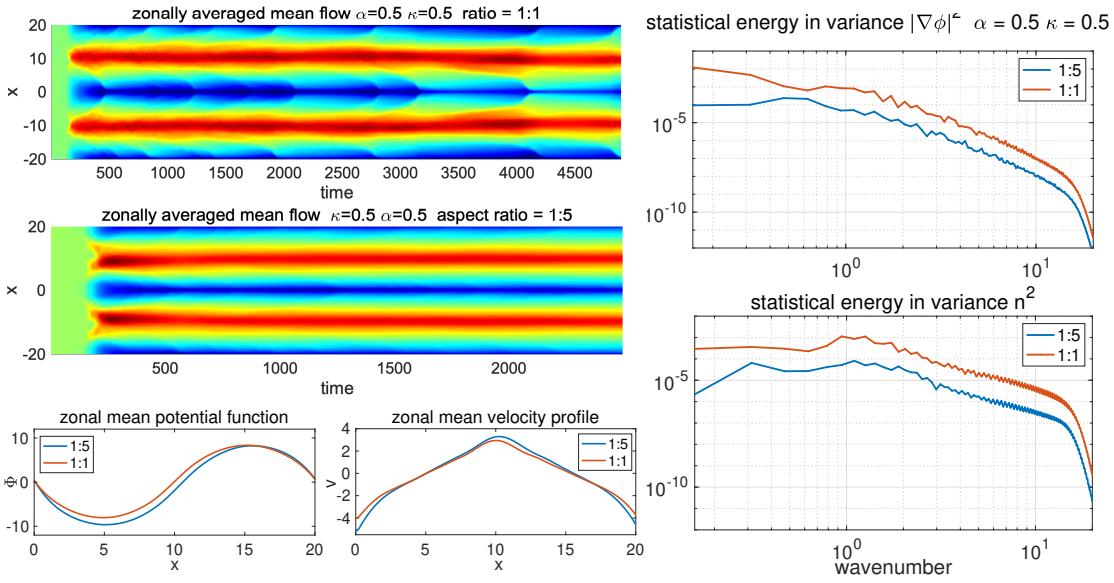

FIG. 6. Time-series of zonal mean flow (upper left) and steady state zonal mean profiles (lower left), and zonal statistical energy spectra in kinetic energy and density (right) with the two different aspect ratios 1:5 and 1:1.

B. Results with extended y poloidal direction

In the final case, we compare the difference in flow variability from an extended channel length $L_y > L_x$. In the previous simulations, we always use equal domain length $L_y = L_x$ with aspect ratio 1. In this simulation, however, we pick a larger aspect ratio $L_y/L_x = 5$, so this represents an elongated channel in the poloidal direction compared with the width in the radial direction. According to the bound for total fluctuations in (23), the factor for the channel length L_y appears in the denominator implying that a longer channel will suppress the fluctuations in the flow field. From the direct numerical simulations, Figure 6 plots the zonal mean profiles in the steady state solutions in $\overline{\varphi}$ and $\overline{v}$, and the time evolutions of the zonal flow $\overline{v}$ with the two aspect ratios 1:1 and 5:1. In agreement with the theoretical prediction, a longer channel domain produces steady zonal flow with nearly no fluctuations compared with the original case with $L_x = L_y$ where more turbulent zonal flow variation is observed. On the other hand, the zonal profile is not affected by the channel domain length. The zonal state structures of the two aspect ratio cases stay similar with each other in a single dominant mode. Besides, we compare the statistical energy spectra of the two cases. Again with a longer channel, the variability among all the scales is effectively suppressed with much smaller variance along the entire energy spectrum in all spectral modes.

V. COMPARING THE BHW AND MHW MODELS IN THE CHANNEL DOMAIN

In this final section, we illustrate the importance of the balanced flux correction in the BHW model (3) by comparing it with the MHW equations without the density correction. First, the MHW model no longer has the non-trivial impulse functions in the channel domain, thus the crucial conserved quantities in the BHW model discussed in Section III are no longer available in the MHW case. Next, the channel domain geometry enables us to discuss the small-amplitude instability generated from an prescribed zonal mean structure. The important difference between BHW and MHW models becomes more obvious from the stability analysis when there exists an linear base state in the zonal density field, where physically consistent instability can be only achieved from the BHW formulation.

A. Lack of non-trivial impulse consesrvation for the MHW equations

The MHW model[18] is formulated by the following dynamical equations for the ion relative vorticity $\zeta = \Delta\varphi$ and the relative ion density n

$$\frac{\partial \zeta}{\partial t} + \nabla^{\perp}\varphi \cdot \nabla \zeta = \alpha\left(\tilde{\varphi} - \tilde{n}\right), \tag{31a}$$

$$\frac{\partial n}{\partial t} + \nabla^{\perp}\varphi \cdot \nabla n + \kappa \frac{\partial \varphi}{\partial y} = \alpha\left(\tilde{\varphi} - \tilde{n}\right). \tag{31b}$$

Again, we consider the inviscid case in the above equations to focus on the nonlinear interactions. A detailed comparison for the dynamical differences in the BHW and MHW models in doubly periodic domain can be found in Ref. 14 and 15 as well as in Refs. 16 and 17 for the role of balanced flux. Here we focus on the role of impulse functions (14) in the MHW formulation important for the analysis in the channel geometry. The corresponding dynamical equations for the zonal states $\overline{\zeta} = \partial_x^2 \overline{\varphi}$ and $\overline{n}$ can be found by zonally averaging the equations (31)

$$\partial_t \overline{\zeta} + \partial_x \left(\overline{\tilde{u}\tilde{\zeta}}\right) = 0,$$

$$\partial_t \overline{n} + \partial_x \left(\overline{\tilde{u}\tilde{n}}\right) = 0,$$

where $\tilde{\zeta} = \nabla^2 \tilde{\varphi}$ and $\tilde{n}$ are the non-zonal fluctuation components. Above the zonal vorticity $\overline{\zeta}$ is the same as the zonal potential vorticity $\overline{q}$ from the BHW model in (8). Therefore for the MHW model, we can also define the impulses from the vorticity and the density field according to the definitions in (14) as

$$I_{\zeta} = \int x\overline{\zeta}, \quad I_n = \int x\overline{n}.$$

However, the corresponding equation for the impulse of vorticity I_ζ can be derived from the zonal equation using the identity in (9) as

$$\frac{dI_\zeta}{dt} = \int \overline{\tilde{u}\tilde{\zeta}} = -\int \partial_x (\tilde{u}\tilde{v}) = 0, \tag{32}$$

where the impulse for ion vorticity $I_\zeta = L\overline{v}_R$ becomes conserved in time. The corresponding equation for the impulse of the density I_n can be found the same as the BHW case

$$\frac{dI_n}{dt} = \int \overline{\tilde{u}\tilde{n}}.$$

In the MHW model case, the impulse for the vorticity I_ζ becomes conserved in time (note that I_ζ here is in the same form as I_q in the BHW model), while the impulse for the density I_n follows the same equation as in the BHW model. This leads to the important difference between the MHW model and the BHW model in the channel geometry. Mathematically, we no longer have the conservation of the total impulse $I = I_\zeta + I_n$. Thus the zonal profiles between the flow potential $\overline{\varphi}$ and the density field $\overline{n}$ cannot be linked together through the conservation law. The important bounds for the zonal relations in the density and flow fields are not guaranteed in the MHW model case. Physically, the conservation of I_ζ in the MHW model requires a constant zonal velocity $\overline{v}_R$ at the right boundary of the channel domain. Thus a time independent constant velocity is maintained along the right boundary.

The lack of impulse conservation illustrated above implies different interaction mechanisms between the zonal states $\overline{n}$ and $\overline{\varphi}$ in the BHW and MHW models. Therefore, it is worthwhile to check in more detail about the effects from a non-zero zonal mean state in the two models. Next, we carry out the linear stability analysis in a similar fashion as in Ref. 24 but based on the existence of a prescribed linear zonal density profile.

B. Linear instabilities due to the zonal density profile in BHW and MHW models

In the analysis of the contribution from the zonal profiles, we consider a single-mode drift wave ($k_y \neq 0$) on top of a zonal mean state in both the velocity field and the density field for BHW ($s = 1$) and MHW ($s = 0$) models

$$\begin{aligned} \varphi &= \hat{\varphi} \exp\left(i\left(\mathbf{k}\cdot\mathbf{x} - \omega t\right)\right) + Vx, \\ n &= \hat{n} \exp\left(i\left(\mathbf{k}\cdot\mathbf{x} - \omega t\right)\right) + Nx, \\ q &= -\left(k^2\hat{\varphi} + \hat{n}\right) \exp\left(i\left(\mathbf{k}\cdot\mathbf{x} - \omega t\right)\right) - Nx\delta_{s0}, \end{aligned} \tag{33}$$

where we introduce a constant zonal mean flow V and an additional linear zonal density profile N. In fact, from the numerical observation in the channel simulations as shown in Figure 4, the assumed linear profile in

the zonal density field Nx is shown a good approximation to the direct numerical solutions. In the potential vorticity $q = \nabla^2\varphi - (\tilde{n} + \delta_{s0}Nx)$, BHW model with $s = 1$ receives no feedback from the mean density profile N, while the MHW model with $s = 0$ gets the additional term due to the zonal density.

1. A physical interpretation for the zonal mean density

First, we can interpret the additional instabilities by consulting the physical meanings in the zonal density profile. In the construction of the Hasegawa-Wakatani models[9,11], the background density profile is defined with the characteristic length scale κ^{-1} so that

$$n \equiv \frac{n'}{n_0(x)},\ n_0 = \exp(-\kappa x),\ x \in [0, L]. \tag{34}$$

The relative density n in the HW equations is defined as the ratio of the absolute density deviation n' over the background density profile n_0. Above all the variables are normalized, and we assume the background density n_0 starts from 1 in the internal regime of the device at $x = 0$ and reaches the right boundary at $x = L$.

In the constant zonal mean structure used in (33), the additional absolute zonal density fluctuation state can be found in the form according to the assumed background profile

$$Nx = \frac{1}{n_0(x)} \int n' dy \Rightarrow \overline{n'}(x) = Nx \exp(-\kappa x).$$

The absolute zonal density $\overline{n'}(0) = 0$ starts from zero in the inner side of the zonal domain, and approaches zero $\overline{n'} \to 0$ again as $x \to \infty$ at the right boundary. According to the above formula, the absolute density $\overline{n'}(x)$ first increases inside the regime $(0, 1/\kappa)$ and decreases in the regime $(1/\kappa, L)$. The entire absolute zonal density field then becomes

$$n_0 + \overline{n'} = (1 + Nx)\exp(-\kappa x),\ x \in [0, L]. \tag{35}$$

We can interpret the *absolute zonal density profile* depending on the sign of the constant zonal mean N according to (35):

- *Linearly decaying zonal mean profile* $N < 0$: negative N in the zonal mean state steepens the total zonal mean state $n_0 + \overline{n'}$. Due to the additional contribution from $\overline{n'}$, the ion density near the boundary regime is even sparser compared with its inner density. Drift wave instability should be induced to create stronger zonal transport in this negative zonal mean case $N < 0$.

- *Linearly increasing zonal mean profile* $N > 0$: positive N in the zonal mean state slows down the decay in the total density towards the boundary. We consider the change of total density within the characteristic length $(0, 1/\kappa)$, where the absolute density fluctuation $\overline{n'}$ reaches its maximum at the value $1/\kappa$.

– With $N < \kappa$, the density deviation is always below the background profile $n_0 > \overline{n'}$ in the range $(0, 1/\kappa)$. The total density $n_0 + \overline{n'}$ is still decreasing along the radial direction. Instability should still be expected but becomes much weaker due to the slower decay along the zonal direction.

– With $N > \kappa$, the density deviation becomes larger than the background profile after $x = \frac{1}{N}$ and generates a flatter zonal density profile. This case with denser ion concentration near the outer regime should withhold the zonal transport, thus there is no drift instability.

2. Growth rate in small amplitude instability by zonal mean density gradient

Above we see from the physical interpretation that the internal instability can be altered a lot by the inclusion of a zonal mean density state N. In the linear stability analysis, we consider the model response to small-amplitude perturbations as the adiabaticity parameter goes to the zero-resistivity limit $\alpha \to \infty$. The BHW model approaches the modified Hasegawa-Mima model[14] with the equilibrium density profile $n_0 \sim \exp(-\kappa x)$ as $\alpha \to \infty$. Therefore, it is reasonable to check the asymptotic performance of the growth rate from the zonal density perturbation on top of the background profile n_0.

We introduce asymptotic expansion of the fluctuation states (33) in the process approaching the adiabatic limit

$$\begin{aligned} \hat{\varphi} =& \varphi_0 + \varphi_1 \varepsilon + o(\varepsilon), \\ \hat{n} =& n_0 + n_1 \varepsilon + o(\varepsilon). \end{aligned} \tag{36}$$

assuming the adiabaticity parameter $\alpha \sim \varepsilon^{-1} \to \infty$ as $\varepsilon \to 0$. The leading order (φ_0, n_0) gives the Hasegawa-Mima state[24] without drift instability. By introducing the shifted frequency in the asymptotic expansion as

$$\omega = \omega_0 + i\sigma_1 + O(\varepsilon), \tag{37}$$

the leading order of the expanded solution can be expressed in the same form for BHW and MHW models as

$$\begin{aligned} \hat{\varphi} =& \varphi_0 e^{\sigma_1 t} e^{-i\omega_0' t} e^{i\left(\mathbf{k}\cdot\mathbf{x} - V k_y t\right)}, \\ \hat{n} =& n_0 e^{\sigma_1 t} e^{-i\omega_0' t} e^{i\left(\mathbf{k}\cdot\mathbf{x} - V k_y t\right)}. \end{aligned}$$

The exponent σ_1 characterizes the leading-order infinitesimal growth rate from the coupling with a zonal mean state. The total dispersion relation ω_0 is mixed with the Doppler shift due to the background zonal flow state $\omega_0 = \omega_0' + k_y V$. This confirms again that both MHW and BHW models are Galilean invariant under the poloidal velocity boost V along y direction[11,14]. In this way, the effect from the zonal mean velocity V can be eliminated

in the dynamical equations. This enables us to focus on the effects from the zonal density profile introduced from the gradient N. Especially, we will consider the leading order growth σ_1 and dispersion ω_0'.

The linearized equations for $\tilde{q} = \nabla^2\tilde{\varphi} - \tilde{n}$ and $\tilde{n}$ by neglecting the nonlinear coupling between fluctuation modes become

$$\begin{aligned} \frac{\partial \tilde{q}}{\partial t} - (\kappa - N\delta_{s0})\frac{\partial \tilde{\varphi}}{\partial y} &= 0, \\ \frac{\partial \tilde{n}}{\partial t} + (\kappa - N)\frac{\partial \tilde{\varphi}}{\partial y} &= \alpha(\tilde{\varphi} - \tilde{n}). \end{aligned} \tag{38}$$

Above the BHW model ($s = 1$) is free from the zonal mean effect in the vorticity equation; while the MHW model ($s = 0$) contains this additional term from N. Direct asymptotic analysis using the expansions (36) and (37) by comparing each order terms of ε gives the dispersion relations for the two models

$$\begin{aligned} \text{BHW}: \quad \omega_0' &= \frac{\kappa k_y}{1+k^2}; \\ \text{MHW}: \quad \omega_0' &= \frac{(\kappa - N)k_y}{1+k^2}. \end{aligned} \tag{39}$$

The dispersion relation for the BHW model is unaltered with the existence of N. In contrast, the dispersion relation in the MHW model is modified by the background density mean N. The difference can be observed from the different equations in (38) for the BHW and MHW models. It is reasonable for the additional density N to adapt the dynamics for density fluctuation $\tilde{n}$. However, the fluctuation part of the vorticity $\tilde{q}$ removing the zonal mean states should not receive further feedbacks from zonal N state.

With the difference in the dispersion relation, we can then calculate the first order growth rate for the two models as

$$\begin{aligned} \text{BHW}: \ \sigma_1 &= \alpha^{-1}\frac{\kappa k_y^2}{(k^2+1)^2}\left(\frac{\kappa k^2}{k^2+1} - N\right), \\ \text{MHW}: \ \sigma_1 &= \alpha^{-1}(\kappa - N)^2\frac{k_y^2 k^2}{(k^2+1)^3}. \end{aligned} \tag{40}$$

The above two formulas reduce to the same form for drift instability[11,24] when there is no additional zonal profile $N \equiv 0$. With non-zero background mean state, there always exists positive linear instability in the MHW model for the non-zonal fluctuation modes $k_y \neq 0$ due to the square term $(\kappa - N)^2$. On the other hand in the BHW model, the additional background density profile can balance and reduce the instability from the balance between $\frac{\kappa k^2}{k^2+1}$ and N.

The above instability analysis for the BHW model can be used to explain the physical interpretation achieved from the observations from absolute zonal profiles. Consistent instability features can be derived directly from (40) in comparison with the physical intuitions in the density decay profiles:

- With a negative zonal density $N < 0$ or a small positive zonal density fluctuation $0 < N < \kappa$, the zonal density decays from the inner regime toward the outer boundary. Accordingly, a positive growth rate (stronger with $N < 0$ and weaker with $0 < N < \kappa$) is induced from the linear instability in drift waves (40) for the BHW model.

- With strong positive density fluctuation $N > \kappa$, the zonal density profile increases toward the boundary. In this case, no instability should be expected in the drift waves as predicted in the stability analysis (40) with $\sigma_1 < 0$ for the BHW model.

In contrast, the MHW model always generates unstable drift waves with $\sigma_1 > 0$ from the linear instability no matter what values of the zonal density N. Especially, the MHW model even generates stronger drift wave instability with a large $N > \kappa$ increasing to higher density toward the boundary. This means that even in the case with reversed zonal density gradient, the MHW model still gives persistent strong unstable drift waves to drive zonal transport.

C. Comparison of the flow simulations from BHW and MHW models

Finally, we compare the flow solutions from direct numerical simulations using the BHW and MHW models. We first show the difference in flow solutions without adding a background density profile $N = 0$. In Figure 7, the snapshots of the flow vorticity $\zeta = \nabla^2 \varphi$ from the BHW and MHW models are compared together with the equilibrium statistical spectra in variance. The BHW model generates stronger variability among the dominant large scale modes compared with the more steady flow with weaker large scale variability in the MHW model. This implies the more turbulent flow features (in both space and time) from the BHW model simulation. The BHW model also suppresses the enormous small scale fluctuations in the density field. The differences are also observed in the direct numerical simulations of the two models on doubly periodic domain case (see Figure 6 and Table I in Ref. 15 for a direct comparison). Furthermore, in the channel domain case, we have the slaving bound estimation (26) confirming that indeed the large-scale modes should contain a much larger variability than all the other smaller scales in the BHW model case.

Next, we compare the simulation results using two different additional zonal density profiles $N = 0.5, 1.5$ on top of the density fluctuation n. Figure 8 compares the time-series of total energy and enstrophy, as well as the statistical energy spectra from both BHW and MHW models. Consistent with the instability analysis in (40), for the BHW model a large positive value of $N = 1.5$ with increasing density toward the boundary should suppress the instability and particle transport, thus lead to flows with decaying total energy and enstrophy in

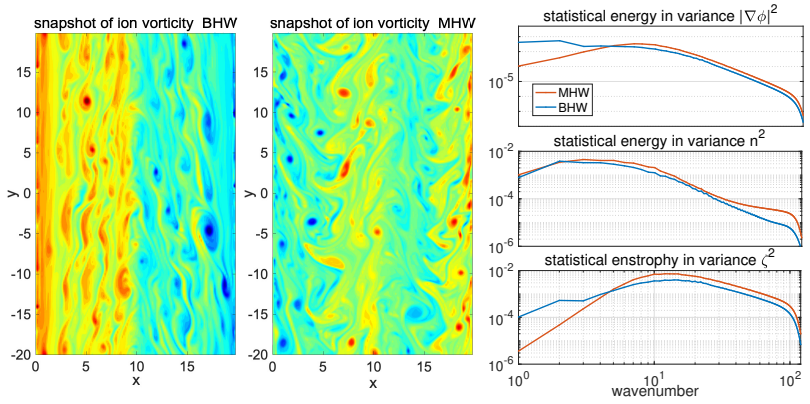

(a) snapshot of ion vorticity (b) energy/enstrophy spectra

FIG. 7. Snapshots of the flow ion vorticity field $\zeta = \nabla^2\varphi$ (left) and the statistical variance spectra (right) from the BHW and MHW model simulations with parameters $\kappa = 1, \alpha = 0.5$.

time from the initial state without turbulence. In contrast, the MHW model still gains instability and develops fully turbulent flow fluctuations on the increasing zonal density profile $N > \kappa$.

In particular in the numerical setup, we pick $N = 0.5, 1.5$ with $\kappa = 1$, so that the growth rate σ_1 for the MHW model becomes the same for the two cases according to the formula (40), and the density gradient N gives uniform effect in the growth rate among all the scales. From the statistical enstrophy spectra on the right panel of Figure 8, the spectra with two distinct values of N display the same shape consistent with the same growth rate, but in contrary to the intuition. In contrast in the BHW model, the density gradient generates different growth rate among different scales. Strong variability especially among small scales will emerge with a small $N = 0.5$ where the zonal density is still decaying towards the right boundary, while a large value of $N = 1.5$ with increasing zonal density profile withholds the zonal transport and induces no fluctuations with much weaker enstrophy.

VI. SUMMARY AND FUTURE WORK

We studied the key characteristics in models for two-dimensional plasma drift wave turbulence on a new channel domain geometry, where a more realistic solid wall boundary condition is introduced along the two sides of the radial direction approximating the tokamak boundaries. The flux-balanced Hasegawa-Wakatani (BHW) model developed in Ref. 14 is reformulated for the channel geometry and is compared with the modified Hasegawa-Wakatani (MHW) model according to the new representative channel flow structures. The efficient pseudo-spectral scheme used in Ref. 15 can be directly adapted to fit the channel domain case for

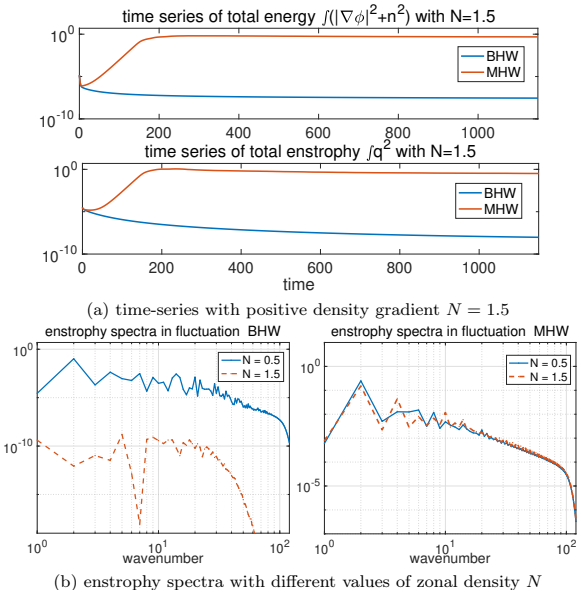

(a) time-series with positive density gradient $N = 1.5$

(b) enstrophy spectra with different values of zonal density N

FIG. 8. Time-series of energy/enstrophy from the BHW and MHW model simulations, and enstrophy spectra with two different values of the zonal density gradients $N = 0.5, 1.5$ in the parameter regime $\kappa = 1$ and $\alpha = 0.5$.

direct numerical simulations of the turbulent channel flows.

Using the channel geometry, we are able to discover richer dynamical features from direct model simulations, and construct a set of new quantities using the impulse functions together with the enstrophy and energy for the analysis of interactions between turbulent fluctuations and zonal flows. The impulse dynamical equations give the total particle flux that can be directly linked to the corresponding enstrophy and energy equations. The combined dynamics provide useful conserved quantities and simplified equations to identify the contributions in zonal and fluctuation states. Many new characterizing properties in the zonal state and fluctuation modes together with their statistical characterization in long time performance can be discovered through this set of new quantities. In addition, the channel geometry enables the introduction of large-scale zonal structures in both flow velocity Vx and density field Nx on top of the disturbance states φ and n. The small perturbations in response to the zonal base state reveal an important advantage of the flux-balanced treatment in the BHW framework with consistent physical intuition. In summary, the following major new features are discovered based on theoretical analysis and numerical simulations of the BHW model:

- The channel domain geometry offers a more physically feasible configuration for the investigation of zonal flow – drift wave interactions in plasma edge turbulence. A new set of conserved quantities can be constructed based on the impulse equations together with the enstrophy and energy on the channel geometry.

- The new conserved quantities help to derive saturation bounds characterizing the maximum growth in total fluctuation modes starting from small initial states. An estimation for the zonal mean state in a dominant wavenumber can also be found based on different values of model parameter κ. The bounds in fluctuations and zonal state are confirmed by directed numerical simulations, and are shown accurate especially in the turbulent regime with large κ.

- The statistical variability in the statistical steady state solutions can be found in the channel domain from the balance between the total particle flux and dissipation effect using the impulse functions. The total statistical variance experiences an abrupt transition as the parameter value κ increases. This is again linked to the amplitude of the dominant zonal mean state and the empirical spectrum structure in zonal modes.

- In addition, flow solutions from different computational domain aspect ratios are compared. A longer channel domain length with extended poloidal y direction is shown to regularize the zonal flow field with much weaker time variability in the jets. This observation is also consistent with the previous theoretical bound estimation.

- The channel domain geometry creates a linear profile Nx in the zonal density field. This zonal density structure in the model construction is confirmed by direct numerical simulations. Through linear instability analysis based on the zonal profile, the BHW model shows consistent growth rates according to the background density according to the signs of N, while the MHW model lacks such correct representation with uniform positive growth rates in both positive and negative density profiles N.

In addition, direct numerical simulations in the channel geometry also display a strong transition in total particle flux as the model parameters change. This shows strong implication for the nonlinear Dimits upshift in the complete quenching of turbulence by zonal flows that have been discussed intensively by many researchers using different models[8,19,20]. Together with the results here and the strategies for analyzing general complex turbulent systems[25–27], the channel domain geometry with the BHW model can serve as a promising framework for the investigation of the Dimits shift and many related interesting phenomena in plasma edge regimes.

ACKNOWLEDGMENTS

This research of A. J. M. is partially supported by the Office of Naval Research N00014-19-S-B001. D. Q. is supported as a postdoctoral fellow on the grant.

REFERENCES

[1]W. Horton, Rev. Mod. Phys. **71**, 735 (1999).

[2]P. H. Diamond, S. Itoh, K. Itoh, and T. Hahm, Plasma Physics and Controlled Fusion **47**, R35 (2005).

[3]Z. Lin, T. S. Hahm, W. Lee, W. M. Tang, and R. B. White, Science **281**, 1835 (1998).

[4]A. Fujisawa, Nuclear Fusion **49**, 013001 (2008).

[5]P. Manz, M. Ramisch, and U. Stroth, Physical review letters **103**, 165004 (2009).

[6]C. Connaughton, S. Nazarenko, and B. Quinn, EPL (Europhysics Letters) **96**, 25001 (2011).

[7]B. Rogers, W. Dorland, and M. Kotschenreuther, Physical review letters **85**, 5336 (2000).

[8]H. Zhu, Y. Zhou, and I. Dodin, Physics of Plasmas **25**, 082121 (2018).

[9]A. Hasegawa and M. Wakatani, Physical Review Letters **50**, 682 (1983).

[10]M. Wakatani and A. Hasegawa, The Physics of fluids **27**, 611 (1984).

[11]R. L. Dewar and R. F. Abdullatif, in *Frontiers in Turbulence and Coherent Structures* (World Scientific, 2007) pp. 415–430.

[12]R. Balescu, *Aspects of anomalous transport in plasmas* (CRC Press, 2005).

[13]W. Horton and A. Hasegawa, Chaos: An Interdisciplinary Journal of Nonlinear Science **4**, 227 (1994).

[14]A. J. Majda, D. Qi, and A. J. Cerfon, Physics of Plasmas **25**, 102307 (2018).

[15]D. Qi, A. J. Majda, and A. J. Cerfon, Physics of Plasmas **26**, 082303 (2019).

[16]D. Qi and A. J. Majda, in press in Chin. Ann. Math., arXiv preprint arXiv:1901.08590 (2019).

[17]D. Qi and A. J. Majda, Journal of Nonlinear Science , 1 (2019).

[18]R. Numata, R. Ball, and R. L. Dewar, Physics of Plasmas **14**, 102312 (2007).

[19]A. M. Dimits, G. Bateman, M. Beer, B. Cohen, W. Dorland, G. Hammett, C. Kim, J. Kinsey, M. Kotschenreuther, A. Kritz, *et al.*, Physics of Plasmas **7**, 969 (2000).

[20]D. A. St-Onge, Journal of Plasma Physics **83** (2017).

[21]A. Majda and X. Wang, *Nonlinear dynamics and statistical theories for basic geophysical flows* (Cambridge University Press, 2006).

[22]D. Qi and A. J. Majda, Journal of Nonlinear Science **28**, 1709 (2018).

[23]A. Hasegawa and K. Mima, The Physics of Fluids **21**, 87 (1978).

[24]D. Qi and A. J. Majda, Physics of Plasmas **26**, 052108 (2019).

[25]A. J. Majda, *Introduction to turbulent dynamical systems in complex systems* (Springer, 2016).

[26]A. J. Majda and D. Qi, SIAM Review **60**, 491 (2018).

[27]A. J. Majda and D. Qi, Chaos: An Interdisciplinary Journal of Nonlinear Science **29**, 103131 (2019).